PNAS

Basaltic reservoirs in the Earth's mantle transition zone

Benoit Tauzin[a,1] , Lauren Waszek[b,c], Maxim D. Ballmer[d] , Juan Carlos Afonso[e], and Thomas Bodin[a]

The formation and preservation of compositional heterogeneities inside the Earth affect mantle convection patterns globally and control the long-term evolution of geochemical reservoirs. However, the distribution, nature, and size of reservoirs in the Earth's mantle are poorly constrained. Here, we invert measurements of travel times and amplitudes of seismic waves interacting with mineralogical phase transitions at 400–700-km depth to obtain global probabilistic maps of temperature and bulk composition. We find large basalt-rich pools (up to 60% basalt fraction) surrounding the Pacific Ocean, which we relate to the segregation of oceanic crust from slabs that have been subducted since the Mesozoic. Segregation of oceanic crust from initially cold and stiff slabs may be facilitated by the presence of a weak hydrated layer in the slab or by weakening upon mineralogical transition due to grain-size reduction.

mantle composition | seismology | mineral physics

Chemical heterogeneities in the form of basaltic and harzburgitic components are introduced into the mantle via the continuous subduction of oceanic plates (1). The resulting spatial compositional variability exerts a strong influence on the dynamics of mantle convection and magma generation. It is also considered the main factor controlling the isotopic diversity of mid-oceanic ridge basalts and lavas from volcanic oceanic islands, which suggests the presence of 2 to 20% recycled crust in the source (2). However, with a melting rate of 5%, the creation globally at ridges of 17 km^3 of basaltic crust per year involves the melting of only 340 km^3/y of mantle. The analysis of primary magma compositions provides an incomplete view regarding global mantle chemistry. Apart from rare ultradeep diamonds with xenolithic inclusions (3), there is little access to the in situ composition at deep upper or mid-mantle depths.

Data on high-pressure mineralogical phase assemblages (4) show that mid-ocean ridge basaltic composition is significantly denser than harzburgite down to 660 km depth but less dense than harzburgite and ambient mantle from 660 to 720 km depth. This density crossover at 660 km depth is thought to promote basalt accumulation near the base of the mantle transition zone (MTZ), but the high viscosity of cold and stiff subducted slabs may prevent efficient separation (segregation) of the basaltic crust from the subducting slab (5, 6). Indeed, there are few indications of anomalous basalt enrichment at MTZ depth near downwellings (7–11), and geodynamic models generally favor segregation near the hot core–mantle boundary (6, 12).

Here, we combine seismic methods and thermodynamic modeling to map out mantle composition at the global scale. We infer mantle temperature and composition via analysis of travel times and amplitudes of compressional (P) and shear (S) waves that have been reflected from the underside of the 410 and 660 km deep discontinuities (PP and SS precursors). This dual approach with global coverage (Fig. 1) improves over recent attempts to document the global distribution of geochemical reservoirs (7–10).

Mantle Chemistry from Seismic Reflection Data

In order to constrain the thermochemical structure of the MTZ, we use two large datasets of 58,217 SS- and 136,512 PP-precursor waveforms. Details about their compilation and the phase and amplitude measurements are described in *Materials and Methods* (see also *SI Appendix*, T1–T3). We analyze the thickness of the MTZ and the amplitudes of P and S wave reflections from the "410" (P410P, S410S) and "660" (S660S). Our data resolution is global (*SI Appendix*, Fig. S1). On average, the MTZ is resolved over a 700-km length scale, and the worst resolution is achieved for PP data in the extreme southern hemisphere (~1,600 km). Such a resolution is enough to discuss the patterns discovered here. The modeling strategy and sensitivity of seismic observables to potential temperature T_{pot} and basalt fraction f are discussed in *Materials and Methods* and described in *SI Appendix*, T4 and T5. T_{pot} and f are assumed to be constant on either side of discontinuities. We make marginal use of P660P reflections as they are hardly visible on seismograms for temperature conditions relevant to the Earth's mantle (13).

Significance

There is no direct access to the deep Earth mantle. Therefore, insights into the deep mantle composition rely on indirect observations from geophysics. We exploit seismic datasets of compressional and shear waves reflected at mineralogical phase transitions globally and reveal the existence of anomalous geochemical reservoirs in the mantle transition zone (MTZ). This first-order compositional pattern is linked to the 100 My old history of tectonic subduction. The existence of basaltic reservoirs and their estimated volumes require mechanisms that allow segregation of the subducted crust from the harzburgitic mantle at mid-mantle depths, regardless of the age of the subducted oceanic lithosphere. Our new constraints on compositional patterns in the MTZ help to understand heat and material flow through the mantle.

In a basalt-harzburgite mixture, the reflectivity (i.e. the amplitudes of reflected waves) at the mineral phase changes from olivine to wadsleyite at the 410 and from ringwoodite to bridgmanite + ferropericlase at the 660 are modulated by the amount of basalt with little effect from temperature (13–15). Conversely, the main parameter controlling MTZ thickness, i.e., the depth difference between the 410 and 660, is the temperature near 410 km depth. This theoretical relationship can be obtained from numerical simulations (*Materials and Methods*) and is shown in Fig. 1 for the S410S and S660S amplitudes at different potential temperatures T_{pot} and basalt fractions f.

Global observations reveal an important contribution from a compositional signature. In Fig. 1, the observed S410S or S660S amplitudes do not just show a subhorizontal trend as a function of the MTZ thickness, as expected for purely thermal variations. Instead, they cover a domain of amplitudes suggestive of basalt fractions of $0 < f < 0.6$. Although predictions do not cover the entire range of observed amplitudes, a similar behavior is reported for P410P (*SI Appendix*, Fig. S2).

As a next step, we inverted the MTZ thickness and S410S, P410P, and S660S reflection amplitudes with a probabilistic framework to constrain (T_{pot}, f) in the MTZ at each geographical location (*SI Appendix*, T6). In order to link temperature and composition to seismic observables via mineral physics modeling, we simulate wave propagation through synthetic mineral aggregates

(*Materials and Methods*). Both observed and synthetic seismic data are processed in the same way. Amplitude data are corrected for the effect of imperfect illumination (incidence angle) and attenuation (*Materials and Methods*). We do not account for out-of-phase stacking due to topography and 3D structure-related focusing/defocusing effects.

In Fig. 2, we present the results of the global inversion of seismic reflection data at each pixel of a 361 × 721 geographical grid. Our global distributions have an average T_{pot} = 1650 K ± 70 K (standard deviation) and f = 0.32 ± 0.1 (Fig. 2 *C* and *D*). Compared with the composition of the uppermost mantle source of mid-ocean ridge basalts, i.e., $f ≈ 0.2$, the MTZ appears globally enriched in basaltic component. Uncertainties on inverted parameters of 40–60 K for T_{pot} and 0.06–0.08 for f (*SI Appendix*, Fig. S10) are mainly due to seismic data coverage. The northern Pacific is notably identified as a region of low uncertainty due to its very dense coverage (*SI Appendix*, Fig. S1).

In addition to the identified global basalt enrichment of the MTZ, one of our key results is that the data require considerable spatial variations of basalt fractions (Fig. 2*B*). The most prominent spatial trend is the relative enrichment in basalt (>50%) in the circum-Pacific region, associated with cold temperatures near recent subduction zones (Fig. 2*A*). This result is robust, as shown by a series of synthetic experiments (*SI Appendix*, T7).
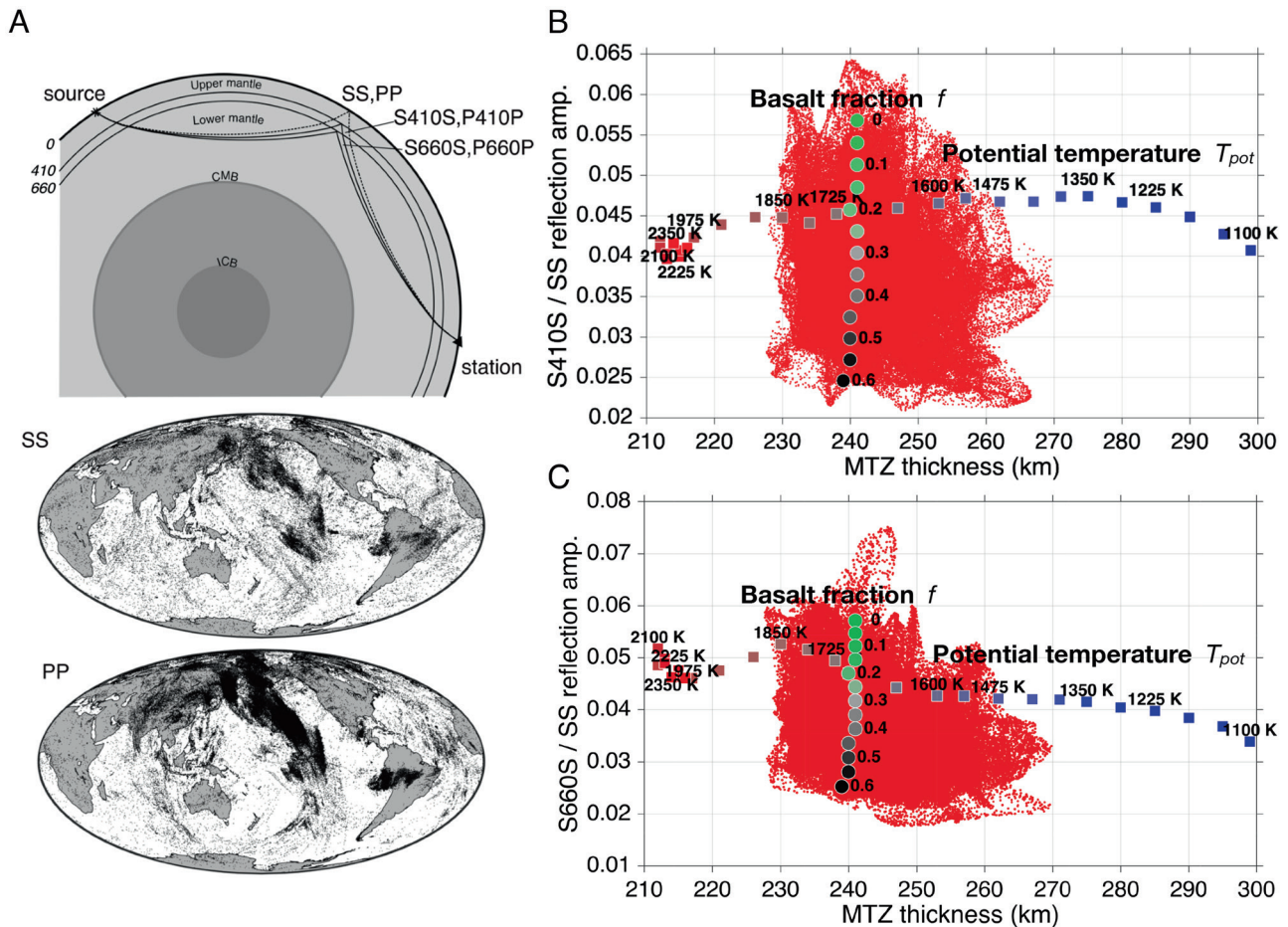

Fig. 1. Seismic reflection data and effects from temperature and chemistry. (*A*) Ray geometry for SS- and PP-precursors and global coverage in reflection points. (*B* and *C*) Diagrams of reflection amplitude ratios for S410S and S660S, as a function of MTZ thickness. Red dots correspond to our global seismic observations (13), sampled over a 361 × 721 geographical grid. Large squares depict theoretical values for a purely thermal case, where the temperature is variable (color of the squares) and the composition is fixed to a mechanical mixture of basalt and harzburgite with basalt fraction f = 0.2 (pyrolitic composition). Large circles depict theoretical values for a purely chemical case, where the basalt fraction varies (color of the circles) and where T_{pot} is fixed to 1,700 Kelvin, close to the global average (13).
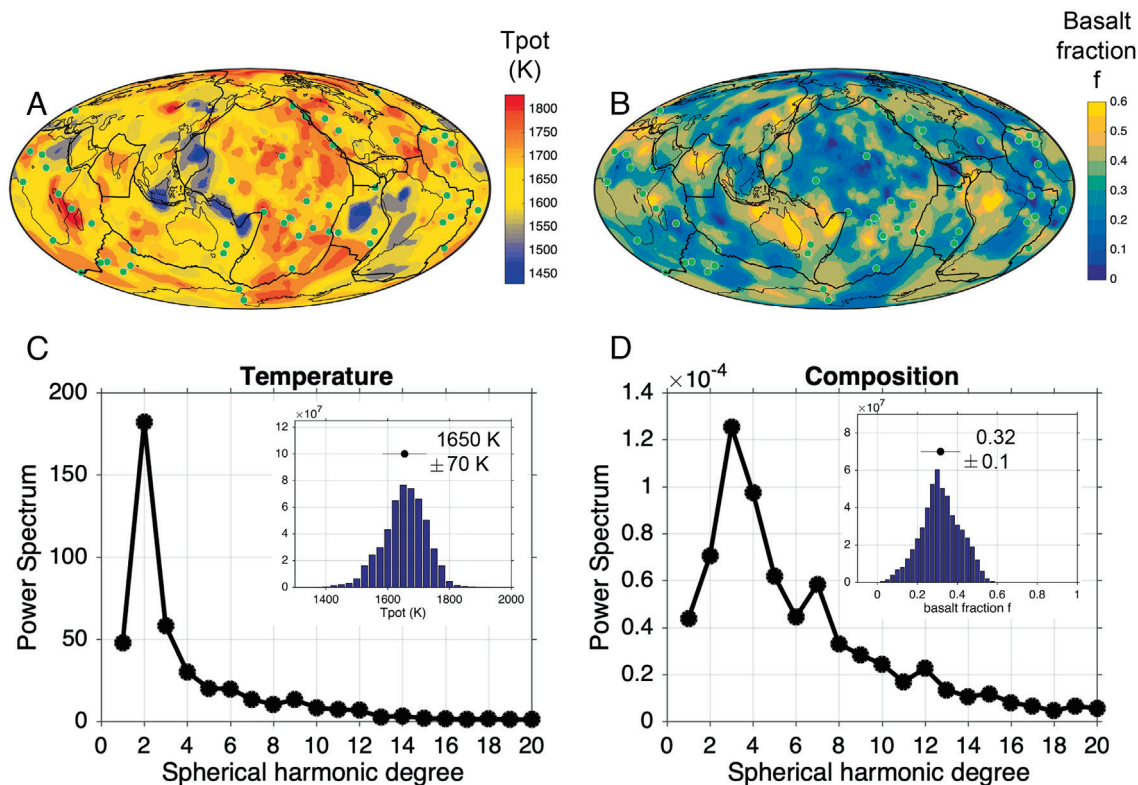
Fig. 2. Patterns and scale of mantle thermal and chemical heterogeneities. Global scale inversion from seismic reflection data allows to recover (*A*) the T_{pot} temperature field and (*B*) the compositional field expressed in terms of basalt fraction *f*. At each geographical location, the variables are represented by Gaussian distributions from which a mean is extracted, as well as a standard deviation (*SI Appendix*, Fig. S10). The T_{pot} and *f* fields are then decomposed over a spherical harmonics basis function, with power spectra plotted as a function of the angular degree in (*C* and *D*). Uncertainties are smaller than the size of the dots. The angular degree *l* is related to the wavelength of heterogeneity $\lambda = 2\pi r_0/l$, where r_0 *is* the radius of the Earth. Degrees *l* = 2, 6, and 15 correspond to wavelengths of 20,000, 6,700, and 2,670 km respectively. Global statistics on model parameters (corrected for cell surface area) are provided as histograms in *Insets*.

The joint inversion of MTZ thickness and reflection amplitudes integrates information on thermochemistry sampled at depths of 410 and 660 km and therefore assumes a constant value for T_{pot} and *f* across the MTZ depth range. An important question is whether the inversion provides a similar pattern of basalt enrichment when using amplitude data that are only sensitive to either the 410 or 660. In *SI Appendix*, Fig. S12, we present inversions that combine the thickness with a single amplitude attribute (either from reflections at the 410 or 660). These inversions reveal patterns of basalt enrichment consistent with those in Fig. 2. The P410P data push the inversion to low basalt compositions (*Materials and Methods*); however, this effect is not dominant. The results of our inversion can be interpreted as weighted radial averages over the thickness of the MTZ. Uncertainties on mineral physics parameters and the presence of volatile elements (e.g., H_2O) have competing effects on estimates of the basalt content (see *Materials and Methods*, and *SI Appendix*, T8).

Validation Using Global Seismic Tomography Models

A change in the spectral character of seismic heterogeneity in the lower mantle has been long known (16–20). The origin of this change remains unclear and has been attributed to various factors such as a viscosity jump (21), a spin transition in iron (22), or volatiles (23). In the following, we argue that variations in the volume and lateral distribution of basalt can explain part of a change in seismic heterogeneity patterns across the 660.

While tomography suffers from poor resolution in the MTZ, our results make a range of predictions that should be expressed

in any tomographic model. Mineral physics modeling (*SI Appendix*, T5) indeed reveals that Δv_s^{600}, the shear-velocity anomaly at 600 km depth, is mainly controlled by T_{pot} with little influence from *f*. Conversely, velocity anomalies at 700 km depth, Δv_s^{700}, are sensitive to both T_{pot} and *f*. Thus, for a purely thermal (i.e., isochemical) model, the correlation between Δv_s^{600} and Δv_s^{700} should be close to perfect. A prediction of such a correlation for a recent thermal model for the MTZ (13) and a constant *f* = 0.2 basalt fraction (*SI Appendix*, Fig. S6) is shown in Fig. 3 (black line with stars). As expected, the correlation between Δv_s^{600} and Δv_s^{700} is almost perfect (+0.96) over all scales. The $\Delta v_s^{600} - \Delta v_s^{700}$ correlation predicted for our thermochemical model presented in Fig. 2 is instead much lower (+0.55), with a sharp decrease at spatial scales *l* = 3–6 (black curve with triangles in Fig. 3), for which the effects of compositional heterogeneity are dominant.

To test for the existence of chemical heterogeneity near the 660 in the MTZ, we use global shear-wave tomographic models from four different research groups (17–20). Correlations are shown in Fig. 3. (See also *SI Appendix*, Fig. S7, for a more systematic comparison at different depths.) Models display drops in correlation suggesting a change in the pattern of heterogeneities across the 660 phase change, consistent with a long-wavelength compositional component. This result suggests that our inferred chemical model is compatible with heterogeneities mapped by independent S-wave models. The differences between velocity models (*SI Appendix*, Fig. S7) stem from the type of data included (e.g., the presence or absence of overtone surface waves), from theoretical assumptions on wave propagation, and from regularization choices made in the tomographic model reconstruction algorithms, such as the parameterization, damping, and smoothing.
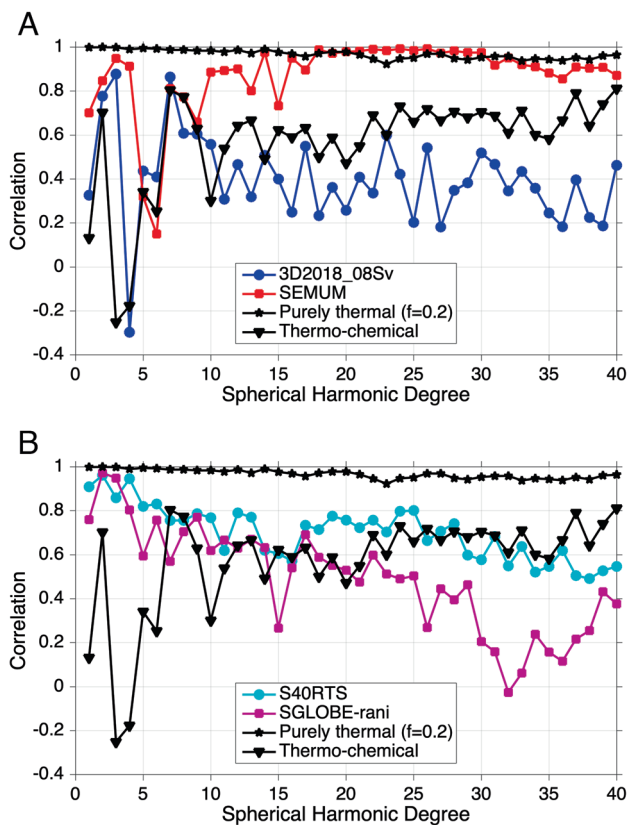
Fig. 3. An indication for the effect of chemistry in seismic tomography data. (*A* and *B*)The correlation between shear-wave speeds at 600 and 700 km depths is shown for a pure thermal model (black line with stars; model from ref. 13) and for velocities derived from our inferred thermochemical model (black line with triangles). Observed correlations are also shown for global tomographic models 3D2018_08Sv (18), SEMUM (20), S40RTS (17), and SGLOBE-rani (19). See *SI Appendix*, Fig. S7 for correlations at other depths.

Taking our analysis a step further, we perform global inversions of the velocity anomalies at 600 and 700 km in tomography models to constrain T_{pot} and f, assuming that these parameters do not vary greatly across the 660-km phase transition (*Materials and Methods*). The results of this inversion together with various sensitivity tests are shown in *SI Appendix*, Figs. S15–S19. While tomography models alone are not the ideal dataset to map out the thermo-chemical structure of the MTZ, the distribution of temperatures (1,667 ± 63 K) and composition (0.29 ± 0.05) are consistent with those inferred from seismic reflection data (*SI Appendix*, Fig. S15). In all models, the inversions confirm that the most enriched basaltic reservoirs are located in the circum-Pacific region (*SI Appendix*, Figs. S15 and S16).

On the Scale of Thermochemical Heterogeneities

Our results demonstrate the presence of regional reservoirs of anomalous mantle composition with increased basaltic component in the vicinity of cold subduction zones, consistent with recent regional observations (8–11). However, our thermochemical models show a difference in the scale of thermal and compositional heterogeneity. The temperature power spectrum is dominated by a $l = 2$ pattern, i.e., a 20,000 km wavelength (Fig. 2*C*). The integrated history of subduction since the Mesozoic is at the origin of such a degree-2 pattern in temperature (24). Subduction likely contributes to the basalt-enrichment associated with the circum-Pacific region (Fig. 2*B*), however patterns in composition

dominate at harmonic degree 3 (Fig. 2*D*) with a relatively "full" spectrum at intermediate degrees up to $l = 6$–7. These smaller-scale patterns cannot be attributed to differences between thermal and chemical diffusion, since the length scale affected by thermal diffusion (~100 km for a 100 My period) is one-to-two orders of magnitude smaller than spatial scales considered here (24). The smaller-scale pattern in composition is likely the signal of basalt segregation and reservoir formation at MTZ depths.

From our measurements, it is difficult to assess the vertical scale of basalt accumulation or the presence of radial discontinuities/gradients in composition. Nevertheless, based on separate inversions of reflection amplitudes (*SI Appendix*, Fig. S12), our analysis reveals similar patterns of basalt enrichment at 410 and 660, indicating that compositional heterogeneity is largely vertically continuous across the MTZ. In detail, the correlation of compositional patterns is strongest for large length scales (degrees < 10), and becomes weaker for smaller scales (*SI Appendix*, Fig. S13).

Time-Integrated History of Subduction

Our new map of MTZ thermo-chemical structure reflects the history of subduction over the last 200 My. Fig. 4 reveals that nearly all regions with a strongly basalt-enriched MTZ ($f > 0.5$) are associated with either present-day subduction or paleo-subduction zones. Notably, eastern Australia is located more than 2,000 km away from present-day subduction zones but is still underlain by a broad basalt-enhanced patch with $f ≈ 0.6$. Plate tectonic reconstructions (e.g., ref. 25) show that the mantle beneath eastern Australia has accumulated large quantities of subducted slabs, with an increased regional slab flux between 60 and 20 Ma.

We conduct a time-integrated analysis of the patterns of composition in relation to subduction since the Mesozoic (*SI Appendix*, T9). We investigate whether a correlation between slab locations and strongly increased basalt fraction is significant and explore how far back in time such a correlation remains visible. We use a global plate motion model (25) and consider the subduction history from 0 to 200 Ma (Fig. 4*A*), over which plate reconstructions are the most robust. The time history in Fig. 4 *B* and *C* reveals that the most basalt-enriched patches are correlated to the subduction history over the last 100 My.

However, our MTZ map shows that not all regions of recent subduction are enriched to the same extent. Furthermore, we find that the MTZ as a whole, including regions far away from recent subduction, is basalt-enriched compared to the pyrolitic mantle average ($f = 0.2$). Indeed, the integrated excess basalt volume in the MTZ in Fig. 4, which we estimate at 1.9 10^{10} km^3, cannot be replenished within 100–150 Ma. For the relevant subduction flux of 3.5–4 km^2/y (26), this volume corresponds to that of all subducted basalt since ~700 Ma, thereby representing a lower bound for its residence timescale in the MTZ. We interpret these results as reflecting two dynamic processes: active basalt segregation in recent (100 ~ 150 Ma) downwelling regions as well as long-term ponding of basalt chunks once segregated due to gravitational trapping (12).

Implications for Mantle Convective Mixing

Our compositional map of the MTZ (Fig. 4*A*) indicates compositional segregation near cold subducting slabs in the MTZ. In general, segregation via gravitational instability is favored by low viscosities and large density contrasts between the basaltic crust and harzburgitic lithosphere (6). Cold slabs are commonly thought to be stiff, and this is the reason why segregation usually
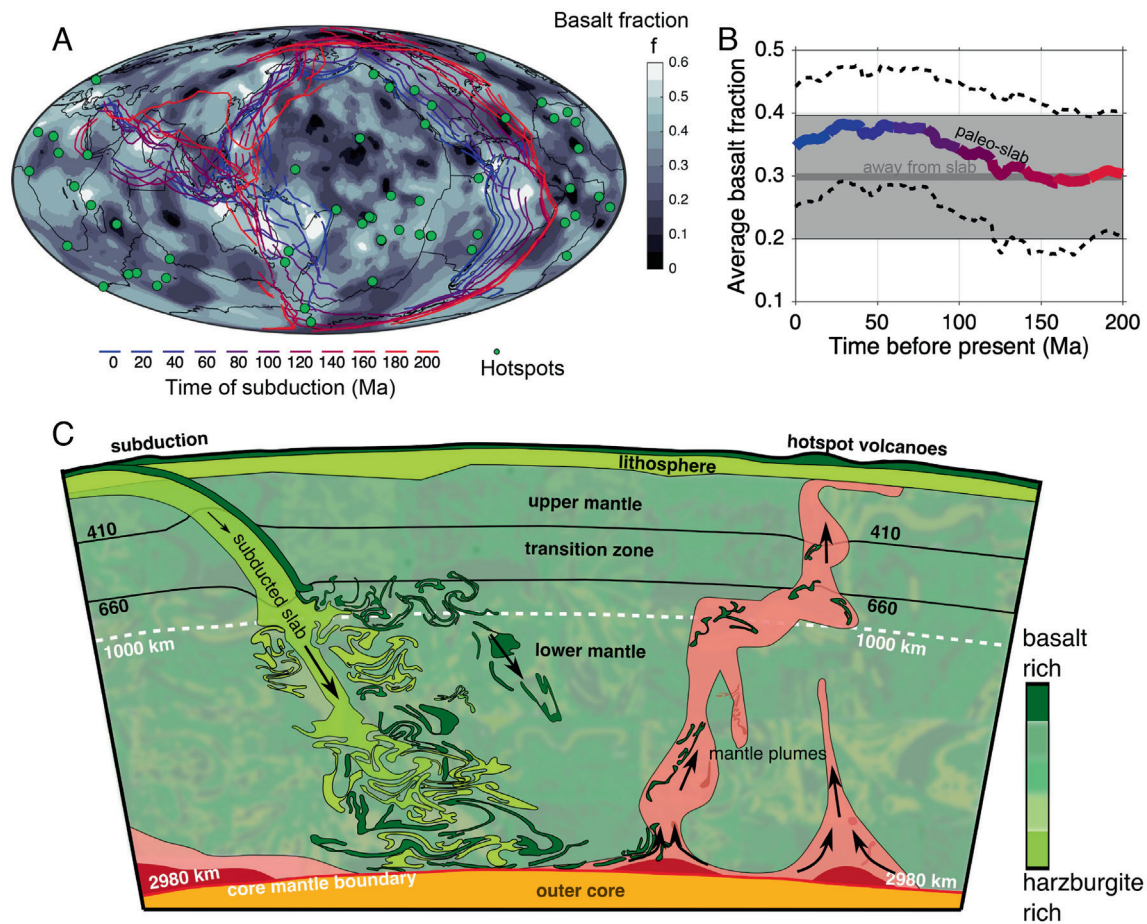
Fig. 4. Effect of tectonic plate subduction since the Mesozoic in the formation of basalt-rich reservoirs. (*A*) Map of our inferred compositional field with superimposed the position of paleo subduction zones (25) from 0 to 200 Ma in intervals of 20 My. Hotspots are marked with green circles. (*B*) Distribution of basalt content (thick colored lines) averaged over the paleo-zones of subduction contours between 0 and 200 Ma. Thick lines and dashed lines show the average and standard deviation of the spatial distribution respectively, and the domain shaded in gray represents the spatial distribution away from paleo subduction zones. (*C*) A sketch depicting the segregation at 660–1,000 km depth of the oceanic crust (dark green) from the harzburgitic component (light green) in a slab and recycling through sinking in the lower mantle and entrainment by a hot plume (light red) rooted at the core–mantle boundary. The "marble cake" composition in the background is inherited from past episodes of mantle convective mixing, oceanic crust separation from the depleted harzburgitic lithosphere, and pooling of the basaltic component within and beneath the transition zone. A small amount of primitive material with anomalous composition is shown with darker red colors near the core–mantle boundary. Segregation could also occur within the MTZ.

does not occur in simplified geodynamic models of slab subduction (5, 6, 12). However, segregation is facilitated by the presence of a weak layer between the basaltic crust and the underlying harzburgite (5). Weakening due to serpentinization and/or hydration likely occurs in the cold slab core (27). Another possibility supported by experiments (e.g., ref. 28) is that the cold slab core may be superweakened due to grain size reduction upon mineralogical phase transition and slow subsequent grain growth. The same weakening mechanism has been attributed to slab buckling, which may further promote segregation near the hinges of slab folds, where basalt layers are stacked and thickened. Segregation of large basalt pools may thus be related to significant slab deformation, such as beneath NE Asia, Tonga-Fiji, or New-Guinea.

A ≥ 700 My minimum residence time of basaltic material in the MTZ (see above) is compatible with predictions from geodynamic models (12). Such a long residence time scale implies that the observed composition of the MTZ (Fig. 2*B*) cannot solely be attributed to present-day subduction, and its interpretation must incorporate the effects of oceanic crust separation integrated over multiple cycles of convective mixing (Fig. 4*C*). The harzburgite–basalt density crossover at the base of the MTZ may provide support for the long-term stability of basalt-rich pools.

According to geodynamic models (4–6, 12), the fate of the largest and most enriched chunks of basalt in the MTZ is to be ultimately flushed into the lower mantle (29) and subsequently accumulate at the core–mantle boundary. Long-time enrichment of the lower mantle in SiO_2-rich basalts is consistent with geochemical signatures (30) and may balance the silica budget of the uppermost mantle (Mg/Si ≈ 1.25) relative to that of planetary building blocks (chondritic meteorites) as well as the Sun's photosphere (Mg/Si ≈ 1.0). Accumulated basalt in the lowermost mantle may then be entrained back by deep-rooted plumes and recycled upward into the mantle (Fig. 4*C*). The amount of basalt carried by plumes depends on plume temperature and basalt density contrast with respect to lower mantle rocks, both poorly constrained. Due to the harzburgite–basalt density crossover, some of this plume-entrained material would replenish a basaltic reservoir in the MTZ (12), with the remainder being sampled at surface "hotspot" volcanism. We potentially detect such a reservoir in the southern Pacific (Fig. 4*A* and *SI Appendix*, Fig. S14), where numerous hotspots are present (Easter, Pitcairn, Marquesas, Tahiti, Society, Cook, and McDonald). Recycling of basalt by plumes into the MTZ may contribute to the large volumes and long residence times inferred above.

While the overall distribution of basalt in the MTZ still indicates dominant delivery by subducted slabs, more detailed analysis of compositional heterogeneity in the mantle will uncover the pathways of material flow through the mantle.

Materials and Methods

Data description and the statistical and modeling frameworks are described in detail in *SI Appendix*. The observed seismic data (*SI Appendix*, T1) originate from (13). We use depth-domain series instead of time-domain series (*SI Appendix*, T2) to remove the effect of bulk velocity heterogeneities on travel-time measurements that mask the effect of temperature onto the depths of mineralogical phase changes. After time-to-depth correction, seismic reflection amplitudes and MTZ thickness data are obtained from an adaptive stacking approach (13), using irregular Voronoi tessellations as described in *SI Appendix*, T2. The use of an irregular parameterization allows global measurements, even in places with poor data coverage, at the price of a decrease in lateral resolution. The global resolution is shown in *SI Appendix*, Fig. S1. Resulting constraints on the MTZ thickness and reflection amplitudes are shown in *SI Appendix*, Figs. S3 and S4. We correct seismic amplitudes for the effect of the incidence angle (*SI Appendix*, T3). Corrections are obtained from full-waveform synthetics (13) and account for the different geometrical spreading of the reference phase (PP/SS) and precursors and further include the influence of anelastic attenuation through the PREM reference model (31). We do not find significant correlation between reflection amplitudes and observed upper mantle quality factors (32, 33). We do not account for out-of-phase stacking due to topography and 3D structure-related focusing/defocusing effects. These factors contribute to decrease measured reflection amplitudes and will bias our inversion results toward higher basalt fractions. We obtain seismic properties for temperatures and compositions through mineral physics modeling (*SI Appendix*, T4) using the code Perple_X (34) and the mineral thermoelastic database from (35) (*SI Appendix*, T2). We tested the new thermoelastic database from reference (36) and found increases of v_p and v_s in the uppermost lower mantle but no significant changes elsewhere. Because of the increased contrast in impedance across the 660, this new database could better explain observed amplitudes for the S660S phase but will not change the adjustment to S410S or P410P phases. Our compositional models are based on mechanical mixtures of the two end-member rock components of the subducted oceanic lithosphere, basalt and harzburgite (37, 38). The sensitivities of seismic observables from reflection and tomography data to (T_{pot}, f) are discussed in *SI Appendix*, T5 and presented in *SI Appendix*, Fig. S8. We use a Bayesian approach (*SI Appendix*, T6) to infer the probability density functions of model parameters $m = (T_{pot}, f)$. In the first case, the data are seismic reflection observables d^{obs} associated with the MTZ thickness h and reflection amplitudes a^{S410S}, a^{P410P}, a^{S660S}, and a^{P660P}. In the second case, the data are velocity anomalies at 600 and 700 km

depths in global tomographic models $d^{obs} = (\Delta v_s^{600}, \Delta v_s^{700})$. We use Bayes' theorem to combine prior information on model parameters with the observed data and obtain the posterior distribution (*SI Appendix*, T6). In *SI Appendix*, T7, we explore the ability of the inversions to recover a uniform pyrolitic mantle composition or a realistic thermo-chemical model and check that the thermal model does leak into the compositional field. We invert for (T_{pot}, f) supposing these are constant across the 410 and 660 phase transitions because inverting for radial changes in composition would give highly nonunique solutions. A basalt fraction that changes across phase transitions would affect seismic reflection amplitudes. In the basalt–harzburgite mechanical mixture, the 660 reflection amplitude is mostly sensitive to the basalt content at the top of the lower mantle. For the 410, there is a trade-off: a decrease of reflection amplitude can be explained either by a general increase of basalt fraction above and below the 410, a sole increase in basalt content in the upper mantle, or an increase in the transition zone. In the case of P410P, part of the amplitude data lie outside of the modeled range (*SI Appendix*, Fig. S2), as mineralogical models do not predict P410/PP amplitudes larger than 4%. Taken with S410S and S660S, the P410P data will push the inversion to low basalt compositions. However, this effect is not dominant. As shown in Fig. 2B and *SI Appendix*, Fig. S12, there are no fundamental differences in the inversion results using or not the PP data, so we chose to present the joint inversion including the PP data (Fig. 2B). Because the new thermoelastic database of (36) increases the 660 impedance contrast (so the S660S reflection amplitude), using such a database would generally increase the prediction of basalt fraction near the 660.

Author affiliations: aLaboratoire de Géologie de Lyon-: Terre, Planètes, Environnement, Université Claude Bernard Lyon 1, Ecole Normale Supérieure de Lyon, Université Jean Monnet, Centre National de la Recherche Scientifique F-69622, Villeurbanne, France; bPhysical Sciences, James Cook University, Douglas, QLD 4811, Australia; cDepartment of Physics, New Mexico State University, Las Cruces, NM 88003; dDepartment of Earth Sciences, University College London, London WC1E 6BS, UK; and eFaculty of Geo-Information Science and Earth Observation, University of Twente, Enschede 7514 AE, the Netherlands

1. C. J. Allègre, D. L. Turcotte, Implications of a two-component marble-cake mantle. *Nature* **323**, 123–127 (1986), 10.1038/323123a0.
2. A. V. Sobolev *et al.*, The amount of recycled crust in sources of mantle-derived melts. *Science* **316**, 412–417 (2007).
3. S. Timmerman *et al.*, Primordial and recycled helium isotope signatures in the mantle transition zone. *Science* **365**, 692–694 (2019).
4. K. Hirose, Y. Fei, Y. Ma, H. K. Mao, The fate of subducted basaltic crust in the Earth's lower mantle. *Nature* **397**, 53–56 (1999).
5. P. E. Van Keken, S. Karato, D. A. Yuen, Rheological control of oceanic crust separation in the transition zone. *Geophys. Res. Lett.* **23**, 1821–1824 (1996).
6. U. R. Christensen, A. W. Hofmann, Segregation of subducted oceanic crust in the convecting mantle. *J. Geophys. Res.: Solid Earth* **99**, 19867–19884 (1994), 10.1029/93JB03403.
7. F. D. Munch, A. Khan, B. Tauzin, M. van Driel, D. Giardini, Seismological evidence for thermochemical heterogeneity in Earth's continental mantle. *Earth Planet. Sci. Lett.* **539**, 116240 (2020).
8. W. Wu, S. Ni, J. C. Irving, Inferring Earth's discontinuous chemical layering from the 660-kilometer boundary topography. *Science* **363**, 736–740 (2019).
9. J. Feng, H. Yao, Y. Wang, P. Poli, Z. Mao, Segregated oceanic crust trapped at the bottom mantle transition zone revealed from ambient noise interferometry. *Nat. Commun.* **12**, 1–8 (2021), 10.1038/s41467-021-22853-2.
10. R. Maguire, J. Ritsema, S. Goes, Evidence of subduction-related thermal and compositional heterogeneity below the United States from transition zone receiver functions. *Geophys. Res. Lett.* **45**, 8913–8922 (2018).
11. F. Bissig, A. Khan, D. Giardini, Evidence for basalt enrichment in the mantle transition zone from inversion of triplicated P-and S-waveforms. *Earth Planet. Sci. Lett.* **580**, 117387 (2022).
12. J. Yan, M. D. Ballmer, P. J. Tackley, The evolution and distribution of recycled oceanic crust in the Earth's mantle: Insight from geodynamic models. *Earth Planet. Sci. Lett.* **537**, 1–12 (2020), 10.1016/j.epsl.2020.116171.
13. L. Waszek, B. Tauzin, N. C. Schmerr, M. D. Ballmer, J. C. Afonso, A poorly mixed mantle transition zone and its thermal state inferred from seismic waves. *Nat. Geosci.* **14**, 949–955 (2021), 10.1038/s41561-021-00850-w.
14. W. Xu, C. Lithgow-Bertelloni, L. Stixrude, J. Ritsema, The effect of bulk composition and temperature on mantle seismic structure. *Earth Planet. Sci. Lett.* **275**, 70–79 (2008), 10.1016/j.epsl.2008.08.012.
15. J. Ritsema, W. Xu, L. Stixrude, C. Lithgow-Bertelloni, Estimates of the transition zone temperature in a mechanically mixed upper mantle. *Earth Planet. Sci. Lett.* **277**, 244–252 (2009).
16. T. W. Becker, L. Boschi, A comparison of tomographic and geodynamic mantle models. *Geochemi. Geophys. Geosyst.* **3**, 1–48 (2002).
17. J. Ritsema, A. Deuss, H. J. Van Heijst, J. H. Woodhouse, S40RTS: A degree-40 shear-velocity model for the mantle from new Rayleigh wave dispersion, teleseismic traveltime and normal-mode splitting function measurements. *Geophys. J. Int.* **184**, 1223–1236 (2011), 10.1111/j.1365-246X.2010.04884.x.
18. E. Debayle, F. Dubuffet, S. Durand, An automatically updated S-wave model of the upper mantle and the depth extent of azimuthal anisotropy. *Geophys. Res. Lett.* **43**, 674–682 (2016), 10.1002/2015GL067329.
19. S. J. Chang, A. M. Ferreira, J. Ritsema, H. J. van Heijst, J. H. Woodhouse, Joint inversion for global isotropic and radially anisotropic mantle structure including crustal thickness perturbations. *J. Geophys. Res.: Solid Earth* **120**, 4278–4300 (2015), 10.1002/2014JB011824.
20. V. Lekic, B. Romanowicz, Tectonic regionalization without a priori information: A cluster analysis of upper mantle tomography. *Earth Planet. Sci. Lett.* **308**, 151–160 (2011), 10.1016/j.epsl.2011.05.050.

21. M. L. Rudolph, V. Lekić, C. Lithgow-Bertelloni, Viscosity jump in Earth's mid-mantle. *Science* **350**, 1349–1352 (2015).

22. G. E. Shephard *et al.*, Seismological expression of the iron spin crossover in ferropericlase in the Earth's lower mantle. *Nat. Commun.* **12**, 1–11 (2021).

23. G. Amulele, S. I. Karato, J. Girard, Melting of bridgmanite under hydrous shallow lower mantle conditions. *J. Geophys. Res.: Solid Earth* **126**, e2021JB022222 (2021).

24. Y. Ricard, M. Richards, C. Lithgow-Bertelloni, Y. Le Stunff, A geodynamic model of mantle density heterogeneity. *J. Geophys. Res.: Solid Earth* **98**, 21895–21909 (1993).

25. A. Young *et al.*, Global kinematics of tectonic plates and subduction zones since the late Paleozoic Era. *Geosci. Front.* **10**, 989–1013 (2019), 10.1016/j.gsf.2018.05.011.

26. M. W. Hounslow, M. Domeier, A. J. Biggin, Subduction flux modulates the geomagnetic polarity reversal rate. *Tectonophysics* **742**, 34–49 (2018).

27. C. T. A. Lee, W. P. Chen, Possible density segregation of subducted oceanic lithosphere along a weak serpentinite layer and implications for compositional stratification of the Earth's mantle. *Earth Planet. Sci. Lett.* **255**, 357–366 (2007).

28. S. I. Karato, M. R. Riedel, D. A. Yuen, Rheological structure and deformation of subducted slabs in the mantle transition zone: Implications for mantle circulation and deep earthquakes. *Phys. Earth Planet. Int.* **127**, 83–108 (2001).

29. P. J. Tackley, D. J. Stevenson, G. A. Glatzmaier, G. Schubert, Effects of an endothermic phase transition at 670 km depth in a spherical model of convection in the Earth's mantle. *Nature* **361**, 699–704 (1993), 10.1038/361699a0.

30. J. M. Tucker, P. E. van Keken, R. E. Jones, C. J. Ballentine, A role for subducted oceanic crust in generating the depleted mid-ocean ridge basalt mantle. *Geochem. Geophys. Geosys.* **21**, e2020GC009148 (2020).

31. A. Dziewoński, D. Anderson, Preliminary reference Earth model. *Phys. Earth Planet. Inter.* **25**, 297–356 (1981), 10.1016/0031-9201(81)90046-7.

32. A. Adenis, E. Debayle, Y. Ricard, Seismic evidence for broad attenuation anomalies in the asthenosphere beneath the Pacific Ocean. *Geophys. J. Int.* **209**, 1677–1698 (2017).

33. H. Karaoğlu, B. Romanowicz, Inferring global upper-mantle shear attenuation structure by waveform tomography using the spectral element method. *Geophys. J. Int.* **213**, 1536–1558 (2018).

34. J. A. Connolly, Computation of phase equilibria by linear programming: A tool for geodynamic modeling and its application to subduction zone decarbonation. *Earth Planet. Sci. Lett.* **236**, 524–541 (2005), 10.1016/j.epsl.2005.04.033.

35. L. Stixrude, C. Lithgow-Bertelloni, Thermodynamics of mantle minerals-II. Phase equilibria. *Geophys. J. Int.* **184**, 1180–1213 (2011), 10.1111/j.1365-246X.2010.04890.x.

36. L. Stixrude, C. Lithgow-Bertelloni, Thermal expansivity, heat capacity and bulk modulus of the mantle. *Geophys. J. Int.* **228**, 1119–1149 (2022).

37. A. Gale, C. A. Dalton, C. H. Langmuir, Y. Su, J. G. Schilling, The mean composition of ocean ridge basalts. *Geochem. Geophys. Geosyst.* **14**, 489–518 (2013), 10.1029/2012GC004334.

38. J. C. Afonso, M. Fernandez, G. Ranalli, W. L. Griffin, J. A. D. Connolly, Integrated geophysical–petrological modeling of the lithosphere and sublithospheric upper mantle: Methodology and applications. *Geochem. Geophys. Geosyst.* **9**, 1–36 (2008), 10.1029/2007GC001834.

39. T. Benoit, L. Waszek, M. D. Ballmer, J. C. Afonso, T. Bodin, A compositional model of the Earth's mantle transition zonefrom SS and PP data [Data set]. Zenodo. https://doi.org/10.5281/zenodo.7198221. Deposited 14 October 2022.

40. L. Waszek, B. Tauzin, N. Schmerr, M. D. Ballmer, J.C. Afonso, Data from "Measurements of the 410 and 660 km discontinuities from global SS and PP precursors." ISC Seismological Dataset. https://doi.org/10.31905/7m3lmg8x. Accessed 9 September 2021.

41. T. Benoit, L. Waszek, Data from "NoLiMit MATLAB package v1.0. Non-Linear Bayesian partition Modeling of the Earth's Mantle Transition zone (Version 1)." Zenodo. https://doi.org/10.5281/zenodo.5512805.Accessed 16 September 2021.

42. B. Tauzin, L. Waszek, J. C. Afonso, Data from "Catalog of synthetic seismic records from mineral physics and travel-time tables." Zenodo. https://doi.org/10.5281/zenodo.5512035. Accessed 16 September 2021.